A MPFA-D FINITE VOLUME SCHEME FOR 2-D SIMULATION OF TWO-PHASE FLOW IN NATURALLY FRACTURED RESERVOIRS USING A LOWER-DIMENSIONAL FRACTURE MODEL

[1]Túlio de Moura Cavalcante

tulio.cavalcante5@yahoo.com

[2]Kelly Cristinne Leite Angelim

kellyangelim01@gmail.com

[3]Braian Schneider Brum

braiansch@hotmail.com

[4]Fernando Raul Licapa Contreras,[5]Paulo Roberto Maciel Lyra, [6]Darlan Karlo Elisiário de Carvalho

ferlicapac@gmail.com, prmlyra@padmec.org, dkarlo101@gmail.com.br

[1,4,5,6] Department of Mechanical Engineering, UFPE, Av. Acadêmico Hélio Ramos s/n, CEP: 50670-901, Recife, PE, Brazil; [2,3]Department of Civil Engineering, UFPE, Av. Acadêmico Hélio Ramos s / n, CEP: 50670-901, Recife, PE, Brazil;

Abstract. *The two-phase flow of oil and water in fractured petroleum reservoirs can be described by a system of nonlinear partial differential equations. Modeling this problem is a great challenge, due to the complexity of the depositional environments including inclined layers, channels, and the random spatial distribution of fractures of different sizes and shapes. In such cases, it is particularly complex to construct structured meshes which are capable of properly model the reservoir. In this work, as far as we know, for the first time, we adapt a cell-centered Finite-Volume Method with a Multi-Point Flux Approximation that uses the so called "diamond stencil" (MPFA-D) to deal with a Lower-Dimensional Fracture Model (LDFM). The MPFA-D is a very robust and flexible that is capable of dealing with highly heterogeneous fractured domains using any polygonal meshes and with full permeability tensor representation for the rock matrix. The LDFM uses an additional equation associated to the fracture which is treated as a geometric entity with a smaller*

Proceedings of the XXXVIII Iberian Latin-American Congress on Computational Methods in Engineering P.O. Faria, R.H. Lopez, L.F.F. Miguel, W.J.S. Gomes, M. Noronha (Editores), ABMEC, Florianópolis, SC, Brazil, November 5-8, 2017.

dimension than the original problem, i.e., for 2-D, fractures have only one dimension in space. This strategy reduces considerably the number of degrees of freedom of the model. The mesh which discretizes the domain must adapt itself to the position and orientation of the fractures, so that these are associated to the control surfaces (edges in 2-D) of the control volumes, therefore, the calculation of the fluxes in these control surfaces is dependent on the pressures in fractures and in the adjacent volumes. The proposed formulation was evaluated by solving some problems given in the literature and by comparing with a similar formulation in which the pressure equation was solved by means of the classical MPFA-O method. Our results are very promising, because, differently from the MPFA-O method, the MPFA-D is a full pressure support method and more robust for highly anisotropic permeability fields.

Keywords: *Two-Phase Flow of Oil and Water, Heterogeneous and Anisotropic Reservoirs, Naturally Fractured Reservoirs, Lower-Dimensional Fracture Model, MPFA-D.*

1 INTRODUCTION

In this paper we present the extension of the cell centered finite volume Multipont Flux Approximation Method with Diamond stencil (MPFA-D), which was originally developed by Gao & Wu (2010) and further adapted for the simulation of two-phase flow in petroleum reservoirs by Contreras *et al.* (2016), coupled with a Lower-Dimensional Fraction Model (LDFM), for the simulation of oil and water displacements in naturally fractured reservoirs. This method is capable of dealing with highly heterogeneous fractured domains by using general polygonal meshes.

The Lower-Dimensional Fracture Model (LDFM) consists of discretizing the fractures as (*n-1*)-dimensional grid cells in an *n*-dimensional domain (Hoteit & Firoozabadi, 2008). This method was presented in context of finite elements by Martin *et al*. (2005) for the modeling of one-phase flow in fractured porous media, and then extended to two-phase flow by Hoteit & Firoozabadi (2008). Later, it was applied together with a MPFA type formulation, by Ahmed *et al*. (2015). For this method, the grid building must be done making the fractures coincide with the control surfaces (edges in 2-D) of the control volumes. In this work, we used the continuous pressure approach.

Comparing with dual-porosity models (Uleberg & Kleppe, 1996), matrix dimension fracture discretization models (Ghorayeb & Firoozabadi, 2000), or even hybrid models (Unsal *et al*., 2010), the LDFM presents computational gains (Hoteit & Firoozabadi, 2008). According to Ahmed *et al*. (2015), the LDFM also presents greater accuracy in relation to other methods for anisotropic fractures and barriers.

This paper presents a MPFA-D formulation that includes the LDFM to solve implicitly pressure equation throughout a fractured petroleum reservoir, coupled with the First Order Upwind Method (FOUM), in an IMPES approach, where the problem of saturation is solved explicitly, on 2-D domains. In order to evaluate the method, we have solved some benchmark problems found in literature, specially comparing its results with some presented in Brum (2016), obtained by a classical type of Multi-Point Flux Approximation which uses triangle pressure support, the MPFA-O (Souza, 2015).

2 MATEMATICAL FORMULATION

In this section, we briefly present the system of nonlinear partial differential equations, composed by one elliptic pressure equation and one hyperbolic saturation equation that are used to model the two-phase flow (oil and water) in heterogeneous porous media. The model considers isothermal flow, incompressible fluid flow and porous media, and that the effects of gravity and capillarity are neglected. From the mass balance (Bear, 1972), we have:

Proceedings of the XXXVIII Iberian Latin-American Congress on Computational Methods in Engineering P.O. Faria, R.H. Lopez, L.F.F. Miguel, W.J.S. Gomes, M. Noronha (Editores), ABMEC, Florianópolis, SC, Brazil, November 5-8, 2017.

$$\phi\rho_i \frac{\partial S_i}{\partial t} + \rho_i \vec{\nabla} \cdot \vec{v}_i = q_i \tag{1}$$

And using the Darcy's Law (Peaceman, 1977; Ewing, 1983):

$$\vec{v}_i = -\lambda_i \underset{\sim}{K} \vec{\nabla} p_i \tag{2}$$

where *i* is the phase index, for water (*w*) or oil (*o*), ϕ is the porosity, *t* is the time variable, $\vec{\nabla}$ is the gradient operator, ρ_i, S_i, $\vec{v}_i$, q_i are, respectively, the phase density, phase saturation, velocity and source term of each phase *i*, λ_i is its mobility, given by the ratio $\lambda_i = k_{ri}/\mu_i$, where k_{ri} is its relative permeability and μ_i is its viscosity. $\underset{\sim}{K}$ is the absolute permeability tensor and p_i is the phase pressure.

Considering that the media only contains oil and water, it is possible to write the following restrictive equation:

$$S_w + S_o = 1 \tag{3}$$

2.1 Pressure Equation

Writing Eq. (1) for both phases and applying the restriction from the Eq. (3) to eliminate the saturation, we get the pressure elliptic equation (Carvalho, 2005) as:

$$\vec{\nabla} \cdot \vec{v} = Q \quad (\text{with } \vec{v} = -\lambda \underset{\sim}{K} \vec{\nabla} p) \tag{4}$$

where $\vec{v} = \vec{v}_w + \vec{v}_o$, is the total velocity and $Q = \sum_i Q_i$, where $Q_i = q_i/\rho_i$. Moreover, $\lambda = \lambda_w + \lambda_o$ is the total mobility and *p* is the global pressure, neglecting capillarity effects.

2.2 Saturation Equation

Taking the Eq. (2) for both phases (oil and water) and multiplying each equation by the mobility of the other phase (Contreras *et al.*, 2016), it becomes as follow:

$$\lambda_w \vec{v}_o = -\lambda_w \lambda_o \underset{\sim}{K} \vec{\nabla} p_o \tag{5}$$

$$\lambda_o \vec{v}_w = -\lambda_o \lambda_w \underset{\sim}{K} \vec{\nabla} p_w \tag{6}$$

Making Eq. (5) – Eq. (6) and later $\vec{v}_o = \vec{v} - \vec{v}_w$, it becomes:

$$\lambda_w \vec{v} - (\lambda_w + \lambda_o)\vec{v}_w = -\lambda_w \lambda_o \underset{\sim}{K} \left(\vec{\nabla} p_o - \vec{\nabla} p_w \right) \tag{7}$$

Reminding that the capillarity effects are neglected, we obtain:

$$\vec{v}_w = \frac{\lambda_w}{(\lambda_w + \lambda_o)}\vec{v} = \frac{\lambda_w}{\lambda}\vec{v} = f_w\vec{v} \tag{8}$$

where f_w is the water fractional flow. So that the Eq. (1) for the water phase is:

$$\phi\frac{\partial S_w}{\partial t} + \vec{\nabla}\cdot(f_w\vec{v}) = Q_w \tag{9}$$

This Eq. (9) is the hyperbolic saturation equation. Equations (4) and (9) are coupled by the total velocity field $\vec{v}$.

2.3 Initial and Boundary Conditions

In order to get a complete description of the problem, it is necessary to define appropriate initial and boundary conditions. In this case, considering a domain Ω, we define the contour Γ as:

$$\Gamma = \Gamma_D \cup \Gamma_N \cup \Gamma_P \cup \Gamma_I \tag{10}$$

where Γ_D and Γ_N represent the boundaries of Dirichlet (prescribed pressure) and Neumann (prescribed flow), respectively, and Γ_P and Γ_I are the production and injection wells, respectively. So that, boundary conditions (Contreras *et al.*, 2016) can be defined as:

$$\begin{aligned}
&\forall\vec{x}\in\Gamma_D \Rightarrow p(\vec{x},t) = g_D \\
&\forall\vec{x}\in\Gamma_N \Rightarrow \vec{v}\cdot\vec{N} = g_N \\
&\forall\vec{x}\in\Gamma_P \Rightarrow p(\vec{x},t) = g_P \\
&\forall\vec{x}\in\Gamma_I \Rightarrow p(\vec{x},t) = g_I \text{ and } S_w(\vec{x},t) = \bar{S}_{w(I)}
\end{aligned} \tag{11}$$

where $\vec{x}$ is defined as the position vector, *t* is time, g_D, g_I and g_P are the scalar functions of pressure and g_N is a scalar function of flux. $\vec{N}$ is the normal vector to the control surface, $\vec{v}$ is the Darcy velocity and $\bar{S}_{w(I)}$ is the set saturation on injection well. Finally, the initial condition is the water saturation field at *t*=0, can be defined as:

$$\forall\vec{x}\in\Omega \Rightarrow S_w(\vec{x},0) = \bar{S}_w^0 \tag{12}$$

3 NUMERICAL FORMULATION

The problem described by Equations (4) and (9), with initial and boundary conditions given by Equations (11) and (12) is solved through the segregated IMPES formulation (IMplicit Pressure Explicit Saturation) (Brum, 2016). In this method, Eq. (4) is solved by an implicit formulation and Eq. (9) is solved by an explicit one.

3.1 Pressure Equation

The discretization of the pressure equation is done through the MPFA-D, initially proposed by Gao & Wu (2010) and further developed by Queiroz *et al.* (2013) and Contreras *et al.* (2016). Therefore, integrating Eq. (4) on a control volume *(CV)* we obtain:

$$\vec{\nabla}\cdot\vec{v} = Q \Rightarrow \int_{\Omega} \vec{\nabla}\cdot\vec{v}\; ds = \int_{\Omega} Q\; dV \tag{13}$$

And from Gauss Divergence Theorem, we have:

$$\int_{\partial\Omega} \vec{v}\cdot\vec{n}\; dA = \bar{Q}V \tag{14}$$

where $\vec{n}$ is the unitary vector normal to the control surface and V is the cell volume (or area, in 2-D grids). Considering a domain or subdomain (grid cell) delimited by a group of segments, and from the mean value theorem, we obtain:

$$\sum_i \vec{v}_i \cdot \vec{N}_i = \bar{Q}V \tag{15}$$

Aiming to obtain the velocity expression for one edge in a generic mesh, we construct the MPFA-D stencil, as suggested in Fig. 1.

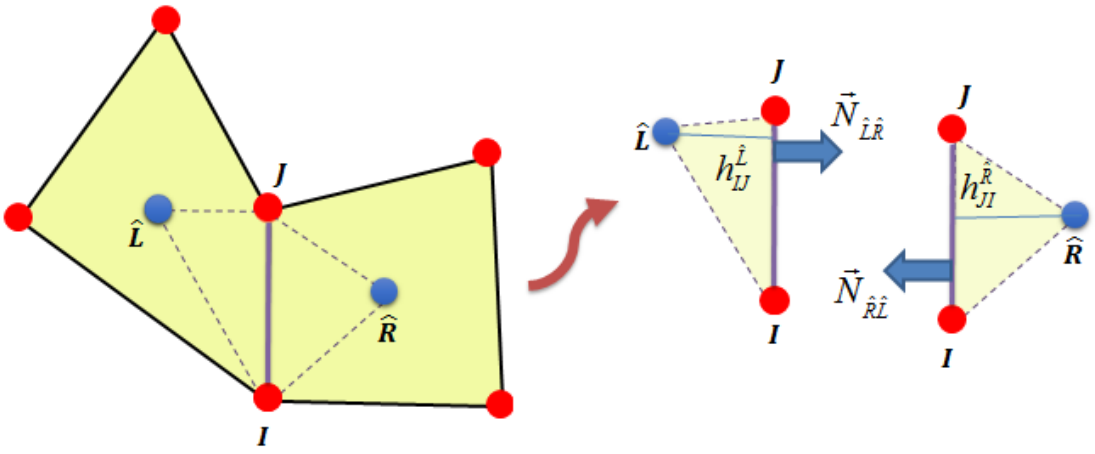

Figure 1: Local diagram of an arbitrary polygonal mesh, illustrating the "diamond stencil".

Considering a 2-D domain and an edge defined by the points *I* and *J*, $\hat{L}$ and $\hat{R}$ denote the barycenters of the cells to the left and to the right of the edge, respectively. The segments $\overrightarrow{IJ}$ and $\overrightarrow{JI}$ are the faces of the cells $\hat{L}$ and $\hat{R}$, respectively. $\vec{N}_{\hat{L}\hat{R}} = \Re\overrightarrow{IJ}$ and $\vec{N}_{\hat{R}\hat{L}} = \Re\overrightarrow{JI}$, such that $\vec{N}_{\hat{R}\hat{L}} = -\vec{N}_{\hat{L}\hat{R}}$ (for the boundary edges, it is used $\vec{N}_{IJ} = \Re\overrightarrow{IJ}$ and $\vec{N}_{JI} = \Re\overrightarrow{JI}$), are the length normal vectors to faces $\overrightarrow{IJ}$ and $\overrightarrow{JI}$, respectively, and $\Re$ is a $\pi/2$ rotation matrix. The heights of the barycenters to the edge are denoted as h_{IJ}^{L} and $h_{JI}^{\hat{R}}$ for the cells $\hat{L}$ and $\hat{R}$,

Proceedings of the XXXVIII Iberian Latin-American Congress on Computational Methods in Engineering
P.O. Faria, R.H. Lopez, L.F.F. Miguel, W.J.S. Gomes, M. Noronha (Editores), ABMEC, Florianópolis, SC, Brazil, November 5-8, 2017.

respectively. $\underset{\sim}{K}\left(\hat{L}\right)=\underset{\sim}{K}_{\hat{L}}$ is the cell permeability in the control volume to the left, what is analogue to the right one. The pressures $p\left(\hat{L}\right)=p_{\hat{L}}$ and $p\left(\hat{R}\right)=p_{\hat{R}}$ are the value approximations in the barycenters of the cells. On the other hand, the pressures $p(I)=p_I$ and $p(J)=p_J$, are the value approximations on the edge vertices.

According to Darcy's law, the velocity crossing through one edge of a grid cell, for example, depends on the permeability, the pressure gradient and the phase mobility on that edge, which, in this paper, is approximated as the arithmetic mean between the total mobilities on the cells which share that edge, as follows:

$$\lambda_{\hat{L}\hat{R}}=\frac{\lambda_{\hat{L}}+\lambda_{\hat{R}}}{2} \tag{16}$$

3.1.1 Flux Calculation

Following the development from Gao & Wu (2010) and Contreras *et al.* (2016), using the diamond pressure stencil, we can write the flux expression as:

$$\vec{v}_{\hat{L}\hat{R}}\cdot\vec{N}_{\hat{L}\hat{R}}=-\lambda_{\hat{L}\hat{R}}K_{\hat{L}\hat{R}}\left|\overrightarrow{IJ}\right|\left[p_{\hat{R}}-p_{\hat{L}}-D_{\hat{L}\hat{R}}\left(p_J-p_I\right)\right] \tag{17}$$

where:

$$K_{\hat{L}\hat{R}}=\frac{K_{\hat{L}}^{(n)}K_{\hat{R}}^{(n)}}{K_{\hat{L}}^{(n)}h_{JI}^{\hat{R}}+K_{\hat{R}}^{(n)}h_{IJ}^{\hat{L}}} \tag{18}$$

$$D_{\hat{L}\hat{R}}=\frac{\overrightarrow{\hat{L}\hat{R}}\cdot\overrightarrow{IJ}}{\left|\overrightarrow{IJ}\right|^2}-\frac{1}{\left|\overrightarrow{IJ}\right|}\left(\frac{K_{\hat{L}}^{(t)}}{K_{\hat{L}}^{(n)}}h_{IJ}^{\hat{L}}+\frac{K_{\hat{R}}^{(t)}}{K_{\hat{R}}^{(n)}}h_{JI}^{\hat{R}}\right) \tag{19}$$

Moreover, we have:

$$K_{\hat{L}}^{(n)}=\frac{\left(\vec{N}_{IJ}\right)^T\underset{\sim}{K}_{\hat{L}}\left(\vec{N}_{IJ}\right)}{\left|\overrightarrow{IJ}\right|^2};\;\; K_{\hat{R}}^{(n)}=\frac{\left(\vec{N}_{JI}\right)^T\underset{\sim}{K}_{\hat{R}}\left(\vec{N}_{JI}\right)}{\left|\overrightarrow{IJ}\right|^2} \tag{20}$$

$$K_{\hat{L}}^{(t)}=\frac{\left(\vec{N}_{IJ}\right)^T\underset{\sim}{K}_{\hat{L}}\left(\overrightarrow{IJ}\right)}{\left|\overrightarrow{IJ}\right|^2};\;\; K_{\hat{R}}^{(t)}=\frac{\left(\vec{N}_{JI}\right)^T\underset{\sim}{K}_{\hat{R}}\left(\overrightarrow{JI}\right)}{\left|\overrightarrow{IJ}\right|^2} \tag{21}$$

The mobilities do not appear in Eq. (19) and Eq. (20), as in Contreras *et al.* (2016), to avoid their entering the harmonic mean calculation, in Eq. (18). Instead, we used the arithmetic mean mobility, from Eq. (16), directly in Eq. (17), to emphasize the contribution of the mobilities in some particular cases, such as fractures, whose model will be presented later in this text. Note that the tangential part of $D_{\hat{L}\hat{R}}$ disappears when the permeability tensor is K-

orthogonal, what makes, in these cases, this MPFA-D scheme becomes a two-point flux approximation formulation (TPFA) (Gao & Wu, 2010).

3.1.2 Boundary Treatment

The treatment of flow over boundaries with prescribed pressures is given by:

$$\vec{v}_{IJ}\cdot\vec{N}_{IJ} = -\lambda_{\hat{L}}\frac{K_{\hat{L}}^{(n)}}{h_{IJ}^{\hat{L}}\left|\overrightarrow{IJ}\right|}\left[\left(\overrightarrow{J\hat{L}}\cdot\overrightarrow{JI}\right)g_D^I+\left(\overrightarrow{I\hat{L}}\cdot\overrightarrow{IJ}\right)g_D^J-\left|\overrightarrow{IJ}\right|^2 p_{\hat{L}}\right]-\left(g_D^J-g_D^I\right)K_{\hat{L}}^{(t)} \tag{22}$$

where $g_D^J = p_J$, $g_D^I = p_I$ are known. When we have prescribed flux over the boundaries (Neumann boundary condition), considering that g_N is the prescribed flux, we can write the flow equation as:

$$\vec{v}_{IJ}\cdot\vec{N}_{IJ} = g_N\left|\overrightarrow{IJ}\right| \tag{23}$$

3.1.3 Treatment of vertex unknowns

Aiming to get a fully cell-centered formulation, it is necessary to interpolate the pressures on each node which are not on Dirichlet boundaries (Fig. 2.a) as a weighted average of the pressures on the centers of the cells which share that node. Following Gao & Wu (2010), it is possible to obtain explicitly the weights of this interpolation, avoiding the inversion of local matrices. Gao & Wu (2010) present two ways to compute the weights in order to produce locally conservative piecewise linear solutions. Following Queiroz *et al*. (2013) and Contreras *et al.* (2016), in our work we restrict ourselves to the type 2 weighting method as shown in Eq. (25). In general, for a vertex *I*, shared by *n(I)* cells, we can write:

$$p_I = \sum_{i=1}^{n(I)} w_{\hat{k}}\, p_{\hat{k}} = w_{\hat{1}}\, p_{\hat{1}} + \cdots + w_{\hat{k}-1}\, p_{\hat{k}-1} + w_{\hat{k}}\, p_{\hat{k}} \tag{24}$$

where $w_{\hat{k}}$ is the weight assigned to the *k*-th cell surrounding the shared node (i.e. weight assigned to p_k). We also define other auxiliary variables ($\overline{k}$) on midpoint of each edge which share node *I*. The pressure on $\overline{k}$, in this work, is going to be considered as arithmetic mean between p_I and p_k (see Figure 2), the pressure on the *k*-th node surrounding *I*. Considering the development from Gao & Wu (2010), and the parameters shown in Fig. 2, the interpolation explicit weights can be computed as:

$$w_k = \frac{\overline{\psi}_k}{\sum_{k=1}^{n(I)}\overline{\psi}_k},\ k = 1,2,...,n(I) \tag{25}$$

where:

$$\bar{\psi}_k = T^{(n)}_{\hat{k},1}\eta_{k,1}\xi_k + T^{(n)}_{\hat{k},2}\eta_{k,2}\xi_{k+1} \tag{26}$$

where:

$$\eta_{k,1} = \frac{\left|\overrightarrow{I\bar{k}}\right|}{h^k_{I\bar{k}}}; \quad \eta_{k,2} = \frac{\left|\overrightarrow{I\bar{k}+1}\right|}{h^k_{I\bar{k}+1}} \tag{27}$$

$$T^{(n)}_{\hat{k},1} = \lambda_{\bar{k}\,\bar{k}-1}\frac{\left(\vec{N}_{I\bar{k}}\right)^T \underset{\sim}{K}_{\hat{k}}\left(\vec{N}_{I\bar{k}}\right)}{\left|\overrightarrow{I\bar{k}}\right|^2}; \quad T^{(n)}_{\hat{k},2} = \lambda_{\bar{k}\,\bar{k}+1}\frac{\left(\vec{N}_{I\bar{k}+1}\right)^T \underset{\sim}{K}_{\hat{k}}\left(\vec{N}_{I\bar{k}+1}\right)}{\left|\overrightarrow{I\bar{k}+1}\right|^2} \tag{28}$$

$$T^{(t)}_{\hat{k},1} = \lambda_{\bar{k}\,\bar{k}-1}\frac{\left(\vec{N}_{I\bar{k}}\right)^T \underset{\sim}{K}_{\hat{k}}\left(\overrightarrow{I\bar{k}}\right)}{\left|\overrightarrow{I\bar{k}}\right|^2}; \quad T^{(t)}_{\hat{k},2} = \lambda_{\bar{k}\,\bar{k}+1}\frac{\left(\vec{N}_{I\bar{k}+1}\right)^T \underset{\sim}{K}_{\hat{k}}\left(\overrightarrow{I\bar{k}+1}\right)}{\left|\overrightarrow{I\bar{k}+1}\right|^2} \tag{29}$$

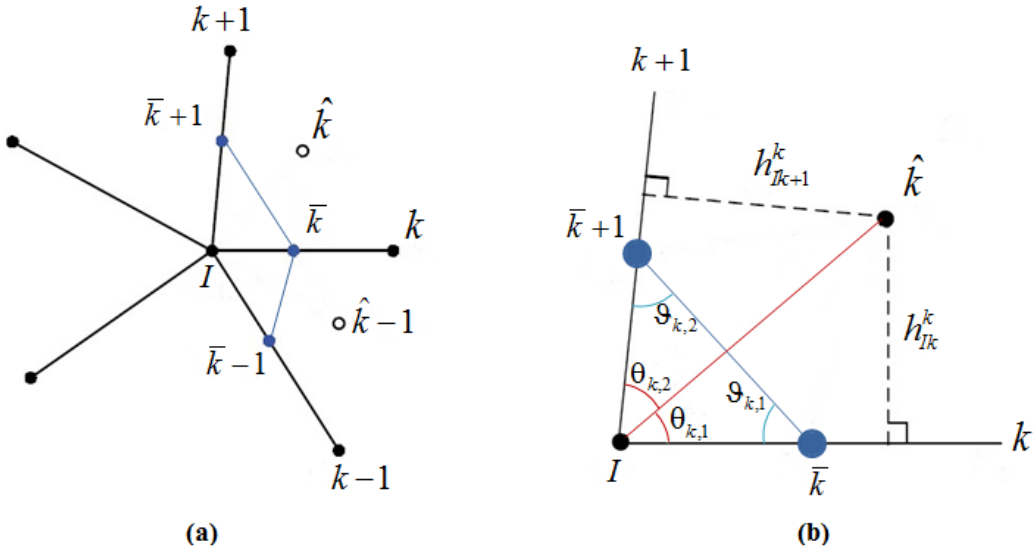

Figure 2: Notation for control volumes (CVs) surrounding the vertex *I*: (a) Notation for CVs, nodes and edges surrounding node *I*. (b) Notation for parameters used to calculate the type 2 explicit interpolation weight, from Gao & Wu (2010), for the *k*-th cell.

where $\lambda_{\bar{k}\,\bar{k}+1}$ is the mobility on the half-edge $\overrightarrow{\bar{k}\;\bar{k}+1}$, analogue to $\lambda_{\bar{k}\,\bar{k}-1}$. And:

$$\xi_k = \frac{\bar{T}^{(t)}_{k-1} - \bar{T}^{(t)}_k + \bar{T}^{(n)}_{k-1}\cot\vartheta_{k-1,1} + \bar{T}^{(n)}_k\cot\vartheta_{k,2}}{T^{(n)}_{\hat{k}-1,2}\cot\theta_{\hat{k}-1,2} + T^{(n)}_{\hat{k},1}\cot\theta_{\hat{k},1} - T^{(t)}_{\hat{k}-1,2} + T^{(t)}_{\hat{k},1}} \tag{30}$$

$$\bar{T}^{(n)}_{\hat{k}} = \lambda_{\hat{k}}\frac{\left(\vec{N}_{\bar{k}\,\bar{k}+1}\right)^T \underset{\sim}{K}_{\hat{k}}\left(\vec{N}_{\bar{k}\,\bar{k}+1}\right)}{\left|\overrightarrow{\bar{k}\;\bar{k}+1}\right|^2} \tag{31}$$

$$\bar{T}^{(t)}_{\hat{k}} = \lambda_{\hat{k}}\frac{\left(\vec{N}_{\bar{k}\,\bar{k}+1}\right)^T \underset{\sim}{K}_{\hat{k}}\left(\overrightarrow{\bar{k}\;\bar{k}+1}\right)}{\left|\overrightarrow{\bar{k}\;\bar{k}+1}\right|^2} \tag{32}$$

where $\lambda_{\hat{k}}$ is the mobility on *k*-th cell surrounding *I*. The angles $\theta_{k,1}, \theta_{k,2}, \vartheta_{k,1}$ and $\vartheta_{k,2}$ are defined as shown in Fig. 2.b.

3.1.4 Lower-Dimensional Fracture Model

In this work, we used the continuous pressure Lower-Dimensional Fracture Model (LDFM) presented in Martin *et al*. (2005), in which the fractures are associated to the control surfaces. It means that it is necessary to build a virtual mesh which will relate to the geometric one. In Fig. 1, we can see that, if, for example, *IJ* is part of a fracture, with a_f as its aperture, the imposition of flux continuity can not be directly applied between *CV*s $\hat{L}$ and $\hat{R}$, because of the tangential flux between fracture-edges. But considering virtual edges between the fracture and the grid cells surrounding it, it becomes clear that the mass conservation is still valid, not between $\hat{L}$ and $\hat{R}$, but between $\hat{L}$ and $\hat{f}$, and between $\hat{f}$ and $\hat{R}$, as shown in Fig. 3.

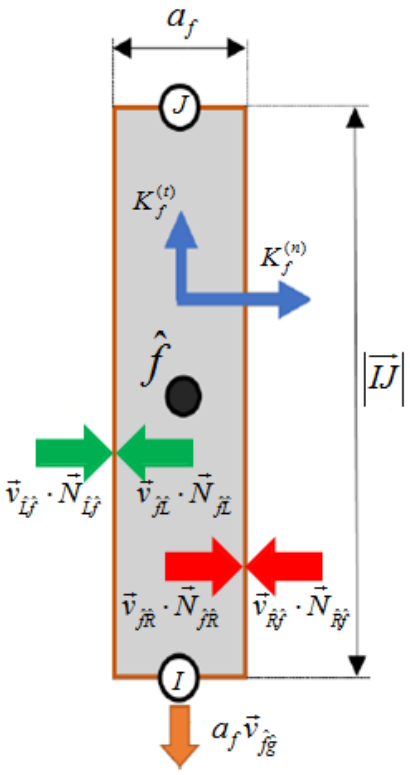

Figure 3: Mass conservation over the virtual edges of one fracture.

Emphasizing that the calculation of the mobility on the virtual face between $\hat{L}$ and $\hat{f}$ follows the idea of Eq. (16), making it to be the arithmetic mean between the mobilities in this two cells, we can rewrite Eq. (17), Eq. (18) and Eq. (19), for this virtual face, as:

$$\vec{v}_{\hat{L}\hat{f}} \cdot \vec{N}_{\hat{L}\hat{f}} = -\lambda_{\hat{L}\hat{f}} K_{\hat{L}\hat{f}} |\overrightarrow{IJ}| \left[p_{\hat{f}} - p_{\hat{L}} - D_{\hat{L}\hat{f}} \left(p_J - p_I \right) \right] \tag{33}$$

$$K_{\hat{L}\hat{f}} = \frac{2K_{\hat{L}}^{(n)}K_f^{(n)}}{K_{\hat{L}}^{(n)}a_f + 2K_f^{(n)}h_{IJ}^{\hat{L}}} \tag{34}$$

$$D_{\hat{L}\hat{f}} = \frac{\overrightarrow{\hat{L}\hat{f}}\cdot\overrightarrow{IJ}}{\left|\overrightarrow{IJ}\right|^2} - \frac{1}{\left|\overrightarrow{IJ}\right|}\left(\frac{K_{\hat{L}}^{(t)}}{K_{\hat{L}}^{(n)}}h_{IJ}^{\hat{L}} + \frac{K_f^{(t)}}{K_f^{(n)}}\frac{a_f}{2}\right) \tag{35}$$

The treatment to the virtual edge between $\hat{R}$ and $\hat{f}$ is analogue. If there is any other fracture-edge sharing the node *I*, for example, there is flux crossing through this vertex (Fig. 4) and it is necessary to make a flow balance on this node, so that, it is necessary to calculate the flux from each fracture-edge to node *I*. Following the same idea from Eq. (16) and Eq. (17), we can write it, for the *k*-th fracture-edge sharing node *I*, as:

$$\vec{v}_{\hat{k}I}\cdot\vec{N}_{\hat{k}I} = -\frac{2K_{\hat{k}}^{(t)}a_k}{E_k}\left[p_I - p_{\hat{k}}\right] \tag{36}$$

where E_k is the length of the fracture-edge. Moreover, it is imposed:

$$\sum_k \vec{v}_{\hat{k}I}\cdot\vec{N}_{\hat{k}I} = 0 \tag{37}$$

where *k* is the index which indicates each fracture surrounding the node *I*. So that, *k=f,g,h* in the example of Fig. 4.b.

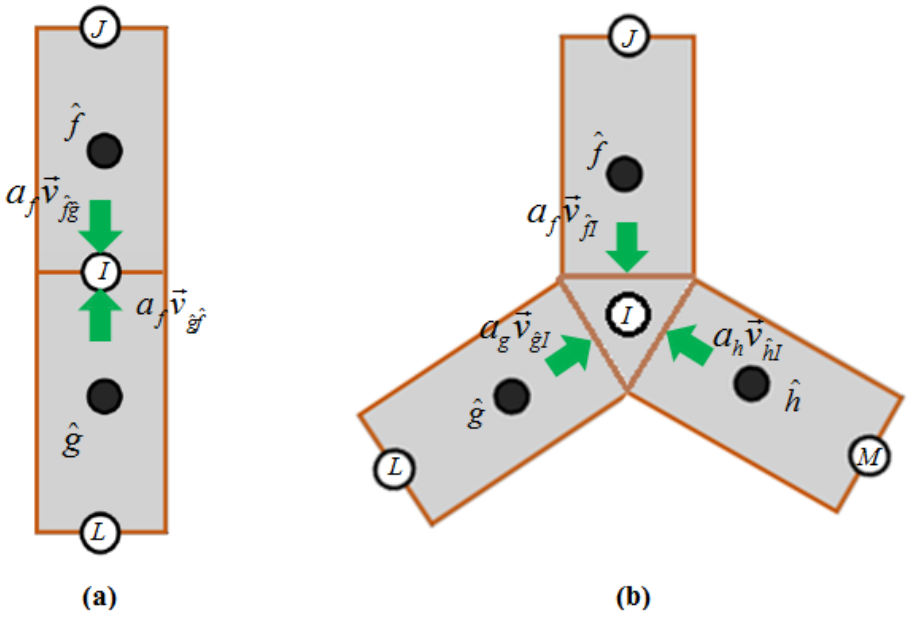

Figure 4: Treatment of a fracture vertex crossing flux. (a) Treatment of the nodes shared by two fracture-edges. (b) Treatment of the nodes shared by more than two fracture-edges.

But, if node *I* is shared by only two fractures with the same aperture (Fig.4.a), the equation (36) and the imposition (37) becomes just as follows:

$$\vec{v}_{\hat{f}\hat{g}} \cdot \vec{N}_{\hat{f}\hat{g}} = -\lambda_{\hat{f}\hat{g}} K_{\hat{f}\hat{g}} a_f \left[p_{\hat{g}} - p_{\hat{f}} \right] \tag{38}$$

where:

$$K_{\hat{f}\hat{g}} = \frac{2K_g^{(t)} K_f^{(t)}}{K_g^{(t)} \left|\overrightarrow{IJ}\right| + K_f^{(t)} \left|\overrightarrow{IL}\right|} \tag{39}$$

About the interpolation weights calculation, if a node to be interpolated belongs to a fracture-edge *f*, the weight of this cell on the interpolation can be calculated just as Eq. (25) and Eq. (26), but with:

$$\eta_{k,1} = \eta_{k,2} = \frac{\left|\overrightarrow{IJ}\right|}{a_f} \tag{40}$$

Considering the local coordinates system defined by $K_f^{(n)}$ and $K_f^{(t)}$, the transmissibility terms becomes:

$$\frac{T_{\hat{f},1}^{(n)}}{\lambda_{\hat{f}\,\hat{f}-1}} = \frac{T_{\hat{f},2}^{(n)}}{\lambda_{\hat{f}\,\hat{f}+1}} = \frac{\begin{bmatrix} \left|\overrightarrow{IJ}\right| & 0 \end{bmatrix} \begin{bmatrix} K_f^{(n)} & 0 \\ 0 & K_f^{(t)} \end{bmatrix} \begin{bmatrix} \left|\overrightarrow{IJ}\right| \\ 0 \end{bmatrix}}{\left|\overrightarrow{IJ}\right|^2} = K_f^{(n)} \tag{41}$$

$$T_{\hat{f},1}^{(t)} = T_{\hat{f},2}^{(t)} = 0 \tag{42}$$

$$\overline{T}_{\hat{f}}^{(n)} = \lambda_{\hat{f}} \frac{\begin{bmatrix} 0 & a_f \end{bmatrix} \begin{bmatrix} K_f^{(n)} & 0 \\ 0 & K_f^{(t)} \end{bmatrix} \begin{bmatrix} 0 \\ a_f \end{bmatrix}}{{a_f}^2} = \lambda_{\hat{f}} K_f^{(t)} \tag{43}$$

$$\overline{T}_{\hat{f}}^{(t)} = 0 \tag{44}$$

Moreover, they are good approximations to consider $\vartheta_{k,1} = \vartheta_{k,2} = \pi/2$ and $\theta_{k,1} = \theta_{k,2} \approx 0$, so it is possible to consider that $\sin\theta \approx \theta = a_f/2$, therefore, $\cot\theta_{k,i} \approx 2/a_f$ and $\cot\vartheta_{k,i} = 0$, for *i*=1,2. So that, the Eq. (30) becomes:

$$\xi_f = \frac{a_f \lambda_{\hat{f}} K_f^{(t)} \cot\vartheta_{f-1,1}}{a_f \lambda_{\hat{f}\,\hat{f}-1} K_{f-1}^{(n)} \cot\theta_{\hat{f}-1,2} + 2\lambda_{\hat{f}\,\hat{f}-1} K_f^{(n)}} \tag{45}$$

3.2 Saturation Equation

Integrating Eq. (9) over *k*-th grid cell, we obtain:

$$\int_{\Omega_k} \phi \frac{\partial S_{w(k)}}{\partial t} \partial\Omega_k + \int_{\Omega_k} \vec{\nabla} \cdot \left(f_w \vec{v} \right) \partial\Omega_k = \int_{\Omega_k} Q_k \partial\Omega_k \tag{46}$$

Using the mean value theorem and the Euler explicit formulation, we obtain:

$$\int_{\Omega_k} \phi \frac{\partial S_{w(k)}}{\partial t} \partial\Omega_k \cong \phi \frac{S_{w(k)}^{n+1} - S_{w(k)}^{n}}{\Delta t} V_k \tag{47}$$

and:

$$\int_{\Omega_k} Q_w \partial\Omega_k = \bar{Q}_w V_k \tag{48}$$

From the Gauss theorem and later considering that the *k*-th grid cell have A_k edges, we obtain:

$$\int_{\partial\Omega_k} \vec{\nabla} \cdot \left(f_w \vec{v} \right) \partial\Omega_k = \int_{\Gamma_k} f_w \vec{v} \cdot \vec{n}_k \partial\Gamma_k \cong \sum_{i=1}^{A_k} f_w \vec{v}_{ki} \cdot \vec{N}_{ki} \tag{49}$$

$$S_{w(k)}^{n+1} = S_{w(k)}^{n} + \frac{\Delta t}{\phi V_k} \left[\bar{Q}_w V_k - \sum_{i=1}^{A_k} f_w \vec{v}_{ki} \cdot \vec{N}_{ki} \right] \tag{50}$$

Which needs to satisfy the stability condition:

$$\Delta t \leq \phi C \frac{\left| \Delta \vec{x} \right|}{\left| \vec{v} \right| \frac{\partial f_w}{\partial S_w^n}} \tag{51}$$

where *C* is the Courant number, $\left| \Delta \vec{x} \right|$ is the distance between the centers of the cells which share an edge, $\left| \vec{v} \right|$ is the velocity on this edge. The Δt needs to be the minimum one, considering all the grid edges.

4 NUMERICAL RESULTS

In this section, we present the results of the application of the continuous pressure model of LDFM coupled with MPFA-D. First, we present a comparison with MPFA-O, using the same model, for solving a one-phase flow problem. Then, we present a comparison between the results obtained by MPFA-D and MPFA-O, in two two-phase flow problems, but, in this case, the latter method is coupled with discontinuous pressure model of LDFM. The results of MPFA-O were get from Brum (2016). All the tests parameters and results are dimensionless.

4.1 One-phase flow in domain with transverse fractures

Aiming to compare the MPFA-D with the MPFA-O, by the continuous pressure model of LDFM, we solved a one-phase flow problem presented in Ahmed *et al.* (2015) and Brum (2016). Consider a domain $\Omega = [0,2] \times [0,1]$, with $p(0,y) = 0$, $p(2,y) = 1$, $\vec{v}(x,0) = 0$ and $\vec{v}(x,1) = 0$ as its boundary conditions, as shown in Fig. 5, where $\underset{\sim}{K}_m$ is the permeability tensor on the matrix, and K_{f_1} and K_{f_2} are the permeabilities on two types of fractures defined as shown in that figure. The permeability tensor on the matrix is:

$$\underset{\sim}{K}_m = \begin{bmatrix} 1 & 0 \\ 0 & 1 \end{bmatrix} \tag{52}$$

In channels, $K_{f_1}^{(n)} = K_{f_1}^{(t)} = 100$ and, in barrier, $K_{f_2}^{(n)} = K_{f_2}^{(t)} = 2x10^{-3}$. Moreover, the aperture of the fractures is $a_f = 0.01$ and we used four types of structured meshes with 4x8, 16x8, 32x16 and 96x48 grid cells. It was made an evaluation of the improvement of the solution with refinement of the mesh. Figure 6 shows that even for the continuous pressure model, on the coarsest mesh, the MPFA-D is capable to capture the effects of permeability discontinuity, despite the not accurate solution for this mesh, what becomes better with refinement, so that for the mesh with 32x16 it is already possible to see clearly the discontinuity step, which is not detectable by the MPFA-O even with the most refined mesh as shown in Fig. 7. This difference occurs probably because the MPFA-D is a full pressure support formulation, while the MPFA-O is a triangle pressure support one.

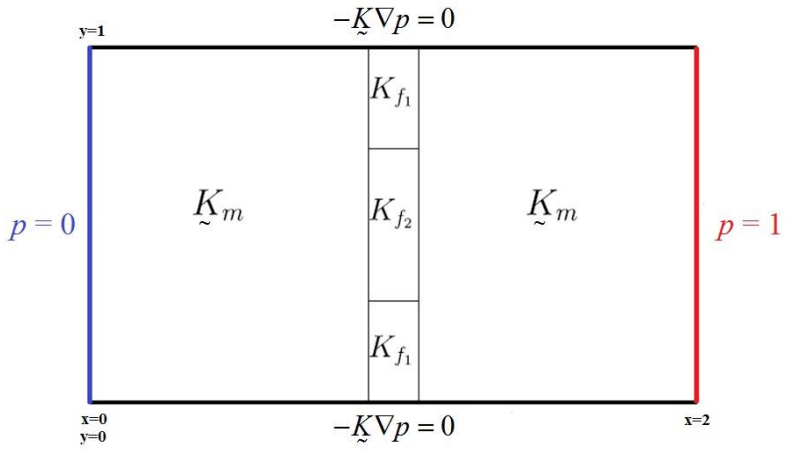

Figure 5: Domain definition with transverse fracture for the one-phase flow problem. Adapted from Ahmed *et al.* (2015).

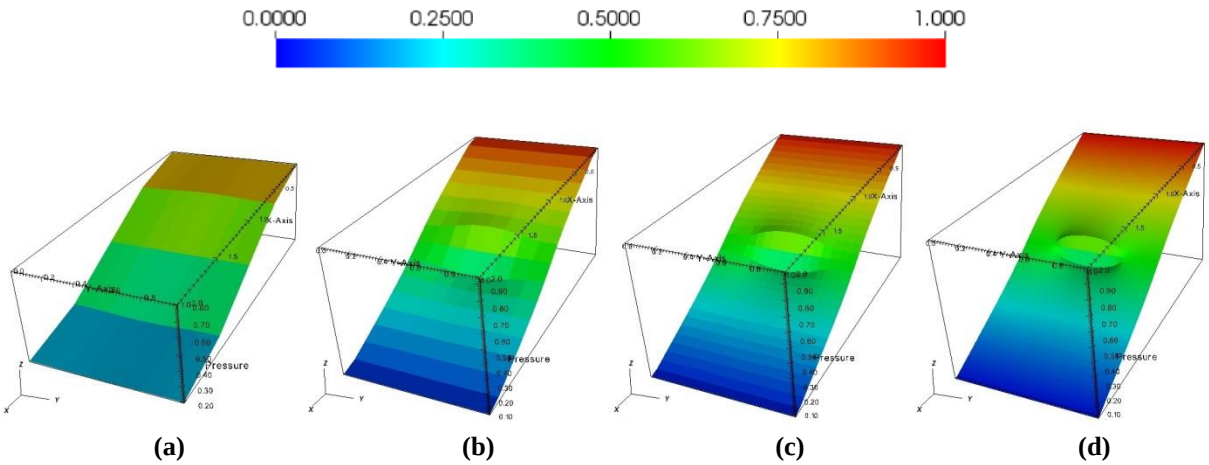

(a) **(b)** **(c)** **(d)**

Figure 6: Solution evolution for one-phase flow problem in domain with transverse fracture considering refinement structured meshes with: (a) 4x8 CVs. (b) 16x8 CVs. (c) 32x16 CVs. (d) 96x48 CVs.

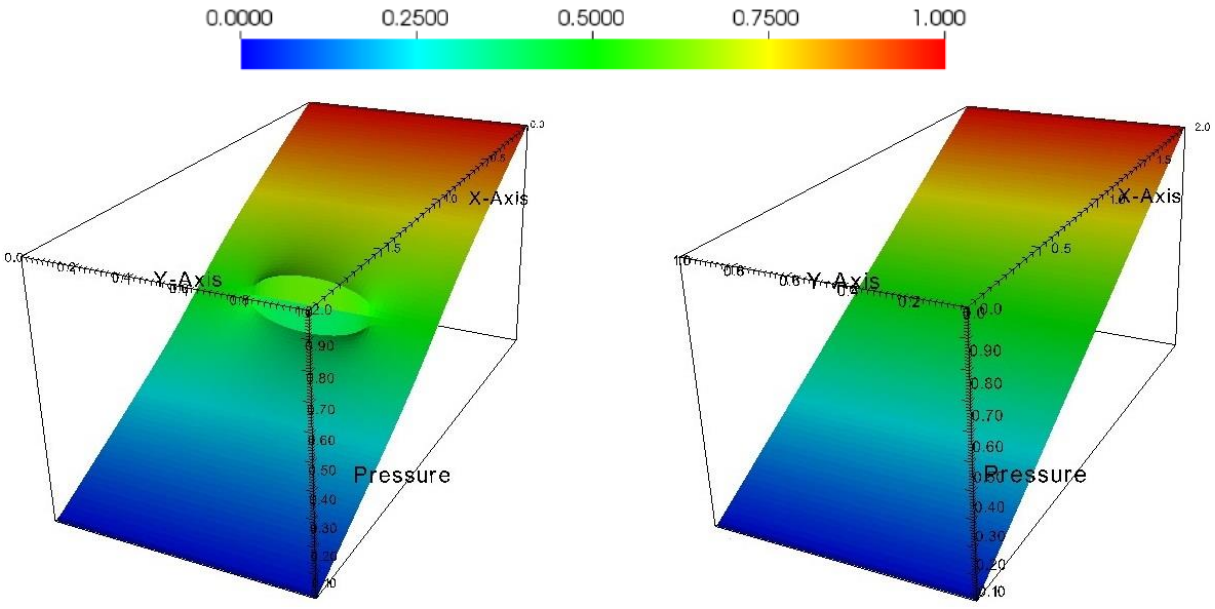

(a) **(b)**

Figure 7: Pressure field for the one-phase flow problem, with continuous pressure model of LDFM, on the structured mesh with 96x48. (a) Result with MPFA-D. (b) Result with MPFA-O.

4.2 The ¼ five spot problem with diagonal fracture

In this example, we solved a two-phase flow problem with diagonal fracture presented in Brum (2016). Consider a domain $\Omega = [0,1] \times [0,1]$, with a diagonal fracture as shown in Fig. 8. There are impositions of no flow crossing through the boundaries, pressure set as $p_P = 0$ on production well and $p_I = 1$ on injection well, and saturation set as $\bar{S}_{w(I)} = 1$ on injection well and $\bar{S}^0_{w(P)} = 0$, initially, on production well. The viscosities of water and oil are 1 and 0.45, respectively, and the permeability on the matrix is:

$$\underset{\sim}{K}_m = \begin{bmatrix} 2 & 1 \\ 1 & 2 \end{bmatrix} \tag{53}$$

On fracture, it is $K_f^{(n)} = K_f^{(t)} = 10^4$. The aperture of fracture is $a_f = 10^{-3}$ and the porosity of the matrix and of the fracture are $\phi_m = 0.2$ and $\phi_f = 1$, respectively. The domain was discretized by an unstructured mesh with 544 points.

Figure 9 and Fig. 10 show, respectively, the water saturation field and the production report for the MPFA-D and the MPFA-O, which is used here as benchmark. These figures show that the MPFA-D presented a satisfactory performance to predict the saturation field configuration, the water breakthrough and cumulate production even using the continuous pressure model.

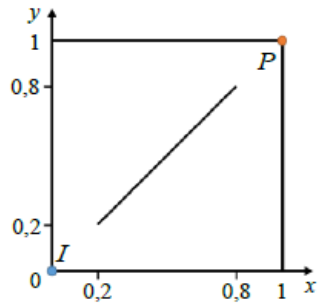

Figure 8: Domain with a diagonal fracture for the ¼ five spot problem. Source: Brum (2016).

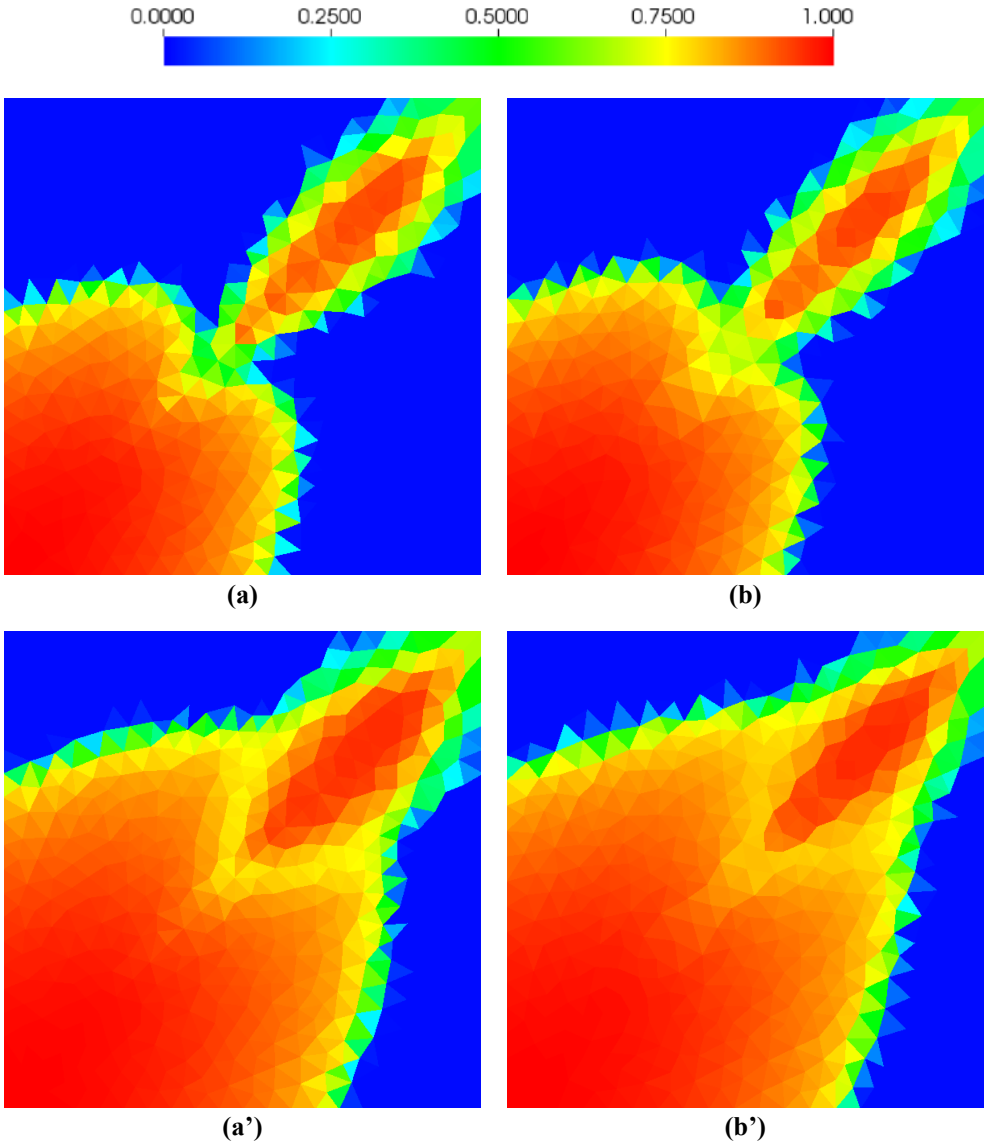

Figure 9: Saturation field for the ¼ five spot problem with diagonal fracture. (a) MPFA-D at 0,5 PVI. (b) MPFA-O at 0,5 PVI, from Brum (2016). (a') MPFA-D at 1,0 PVI. (b') MPFA-O at 1,0 PVI, from Brum (2016).

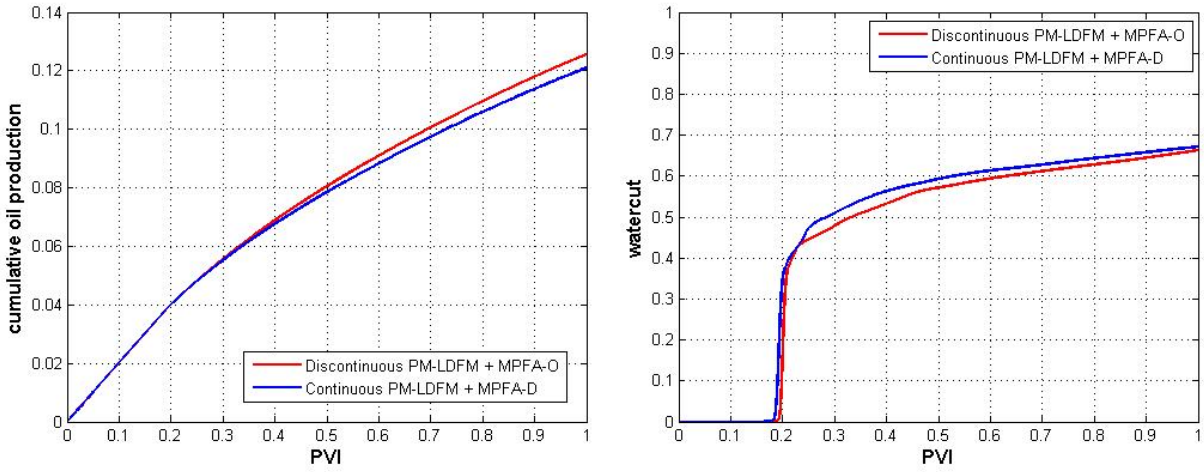

(a) **(b)**

Figure 10: Production Report for the ¼ five spot problem with diagonal fracture. (a) Cumulative oil Production. (b) Watercut.

4.3 The ¼ of five spot problem with connected fractures

We solved another two-phase flow problem of Brum (2016). Consider a domain $\Omega = [0,100] \times [0,100]$, with connected channel and barriers as shown in Fig. 11. The domain was discretized by an unstructured mesh with 71 points. We did not use more refined meshes because it would be very computationally costly (excessively time consuming) to solve it by the IMPES strategy, because the very small fracture aperture in this case pulls down the time step limitation calculated by Eq. (51) so that, in case of more refined meshes, it would take the total time of simulation for days.

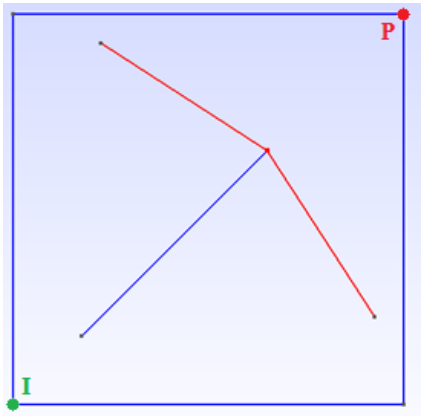

Figure 11: Domain configuration for the ¼ of five spot problem with connected fractures.

There are the impositions of on flow crossing through the boundaries, pressure set as $p_P = 0$ on production well and $p_I = 1$ on injection well, and saturation set as $\bar{S}_{w(I)} = 1$ on injection well and $\bar{S}^0_{w(P)} = 0$, initially, on production well, the viscosities of water and oil are both 1, and the permeability on the matrix is:

$$\underset{\sim}{K}_m = \begin{bmatrix} 10^{-5} & 0 \\ 0 & 10^{-5} \end{bmatrix} \tag{54}$$

On fracture (the blue one), the permeability is $K_{f_1}^{(n)} = K_{f_1}^{(t)} = 800$, and on barriers (red ones) it is $K_{f_2}^{(n)} = K_{f_2}^{(t)} = 10^{-23}$. The aperture of fracture and barriers is $a_f = 10^{-4}$ and the porosity of the matrix and of the fractures and barriers are $\phi_m = 0.2$ and $\phi_{f_1} = \phi_{f_2} = 1$, respectively.

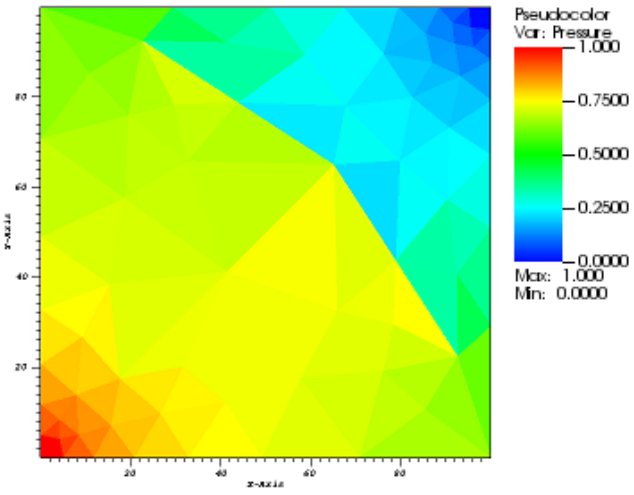

Figure 12: Pressure field for the ¼ of five spot problem with connected fractures.

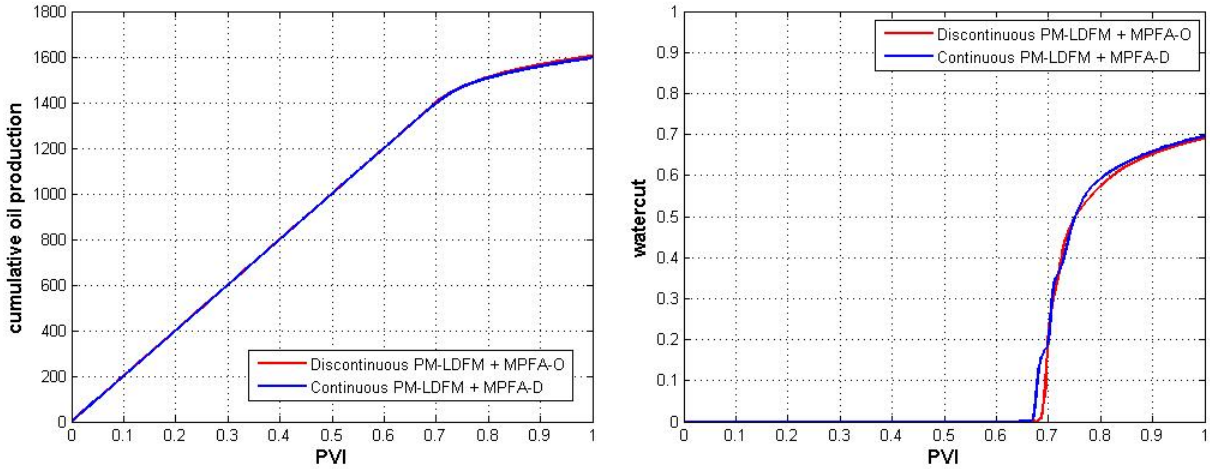

(a) **(b)**

Figure 13: Production report for the ¼ of five spot problem with connected fractures. (a) Cumulative oil production. (b) Watercut.

The resulting pressure field is shown in Fig. 12, where it can be seen the discontinuity in pressure field caused by the presence of the barrier, which can be captured by MPFA-D even with the continuous pressure model of LDFM. The production report had also satisfactory results in comparison with those of MPFA-O, as it is shown in Fig. 13.

5 CONCLUSIONS

In this work, we present a numerical formulation for the simulation of the two-phase fluid flow in naturally fractured petroleum reservoirs. The formulation is based upon a Lower Dimensional Fracture Model using a continuous pressure approach in which the pressure equation is discretized by means of a full pressure support non-orthodox Multipoint Flux Approximation Method with a Diamond Stencil (MPFA-D) and the saturation equation was spatially discretized by the First Order Upwind Method (FOUM). The MPFA-D demonstrated to be capable to capture the effects of the abrupt permeability change through barriers, even for the simple continuous pressure model, returning very good results, consistent with those obtained with the discontinuous pressure model solved using the classical MPFA-O method. In the near future, we intend to implement a discontinuous pressure model using the MPFA-D formulation, which can be particularly more accurate due to the improvement of the treatment of fractures with strong contrast in permeability in comparison to the rock matrix. Besides, we also intend to implement a sequential implicit formulation, in which the saturation equation is also solved implicitly, in order to circumvent the time step limitations of the IMPES procedure.

ACKNOWLEDGEMENTS

The authors thank the Federal University of Pernambuco (UFPE), the Foundation for Support of Science and Technology of Pernambuco (FACEPE), the National Council for Scientific Development (CNPq), and the CENPES-PETROBRAS.

REFERENCES

Ahmed, R., Edwards, M.G., Lamine, S., Huisman, B.A.H., & Pal, M., 2015. Control-volume distributed multi-point flux approximation coupled with a lower-dimensional fracture model, *Journal of Computational Physics*, vol. 284, pp. 462–489.

Bear, J., 1972. *Dynamics of Fluids in Porous Media*. Dover Publications Inc., New York.

Brum, B. S., 2016. *Simulação do Escoamento Bifásico de Água e Óleo em Reservatórios de Petróleo Naturalmente Fraturados Utilizando Métodos de Volumes Finitos Acoplados a Modelos de Fraturas com Dimensão Reduzida*, Dissertação de Mestrado, Universidade Federal de Pernambuco/Recife.

Carvalho, D. K. E., 2005. *Uma Formulação do Método dos Volumes Finitos com Estrutura de Dados por Aresta para a Simulação de Escoamentos em Meios Porosos*, Tese de Doutorado, Universidade Federal de Pernambuco/Recife.

Contreras, F. R. L., Lyra, P. R. M., Souza, M. R. A., & Carvalho, D. K. E., 2016. A cell-centered multipoint flux approximation method with a diamond stencil coupled with a higher order finite volume method for the simulation of oil–water displacements in heterogeneous and anisotropic petroleum reservoirs, *Computers & Fluids*, vol. 127, 1–16.

Ewing, R. E., 1983. *The Mathematics of Reservoir Simulation*. Richard E. Ewing ed., Frontiers in Applied Mathematics, vol. 1, SIAM, Philadelphia.

Gao Z., & Wu J., 2010. A Linearity Preserving Cell-Centered Scheme For The Heterogeneous And Anisotropic Diffusion Equations On General Meshes. *International Journal For Numerical Methods In Fluids*, vol. 67, pp. 2157–2183

Ghorayeb, K., & Firoozabadi, A., 2000. Numerical study of natural convection and diffusion in fractured porous media, *SPE Journal*, vol. 5(1), pp. 12–20.

Hoteit, H., & Firoozabadi, A., 2008. An efficient numerical model for incompressible two-phase flow in fractured media, *Advances in Water Resources*, vol. 31(6), pp. 891–905.

Martin, V., Jaffré, J., & Roberts, J.E., 2005. Modelling fractures and barriers as interfaces for flow in porous media, *SIAM Journal on Scientific Computing*, vol. 26(5), pp. 1667–1691.

Peaceman, D. W., 1977. *Fundamentals of Numerical Reservoir Simulation*, Elsevier Scientific Publishing Co., Developments in Petroleum Science, vol. 6, Amsterdam.

Queiroz, L. E. S., Souza, M. R. A., Contreras, F. R. L., Lyra, P. R. M., Carvalho, D. K. E., 2013. On the accuracy of a nonlinear finite volume method for the solution of diffusion problems using different interpolations strategies. *International Journal For Numerical Methods In Fluids*, DOI: 10.1002/fld.

Souza, M. R. A., 2015. *Simulação Numérica de Escoamento Bifásico em Reservatórios de Petróleo Heterogêneos e Anisotrópicos Utilizando um Método de Volumes Finitos "Verdadeiramente" Multidimensional com Aproximação de Alta Ordem*, Tese de Doutorado, Universidade Federal de Pernambuco/Recife.

Uleberg, K., & Kleppe, J., 1996. Dual porosity, dual permeability formulation for fractured reservoir simulation, *Trondheim RUTH Seminar*, Norwegian University of Science and Technology/Stavanger.

Unsal, E., Matthäi, S.K., & Blunt, M.J., 2010. Simulation of multiphase flow in fractured reservoirs using a fracture-only model with transfer functions, *Computational Geosciences*, vol. 14(4), pp. 527–538.